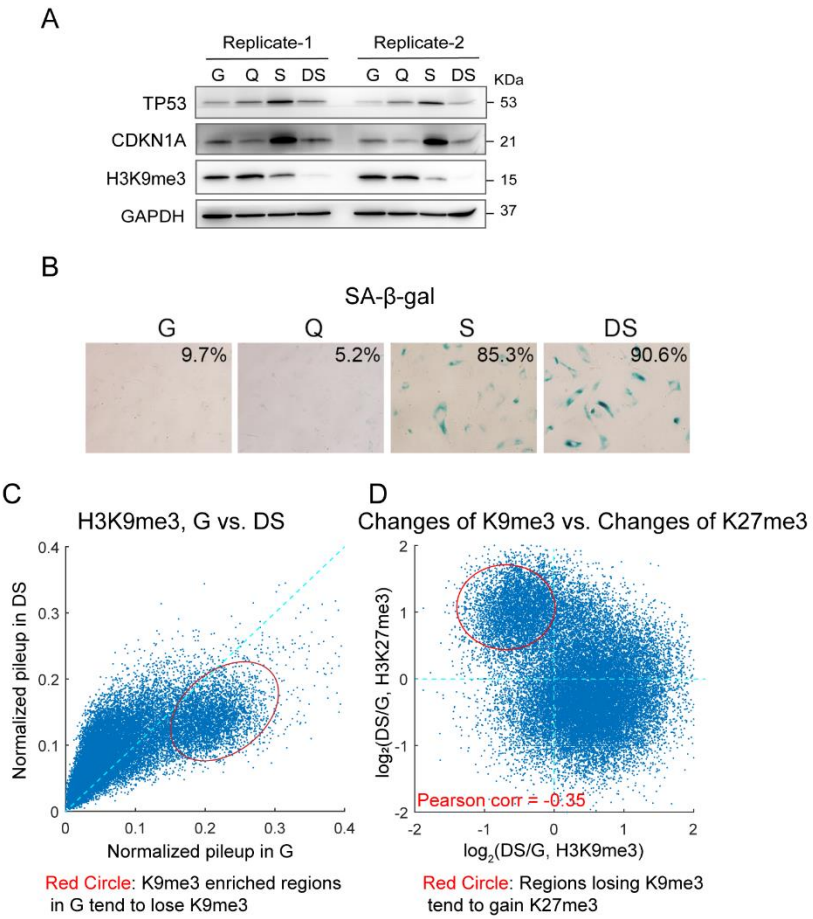

Figure S1. Biological experiment verification of senescence and the loss of heterochromatin phenotype

(A) Western-blot of TP53 (known as p53), CDKN1A (known as p21), H3K9me3 in G, Q, S and DS. Western-blot is performed in two biological replicates. GAPDH were used as control. Protein levels of TP53 and CDKN1A increased in S and decreased in DS. H3K9me3 decreased during senescence.

(B) SA-β-gal staining for four different cell states. The percentage of stained cells were labeled.

(C) Scatter plot of normalized H3K9me3 pileup in G and DS. H3K9me3 enriched regions in G tend to lose H3K9me3 in DS. Notably, ChIP-seq used here were not quantitative.

(D) The Scatter plot of fold changes of H3K9me3 and H3K27me3 between DS and G. Changes of H3K9me3 are negatively correlated with changes of H3K27me3 (r = -0.35). It means Regions losing H3K9me3 during senescence tend to gain H3K27me3 relatively.

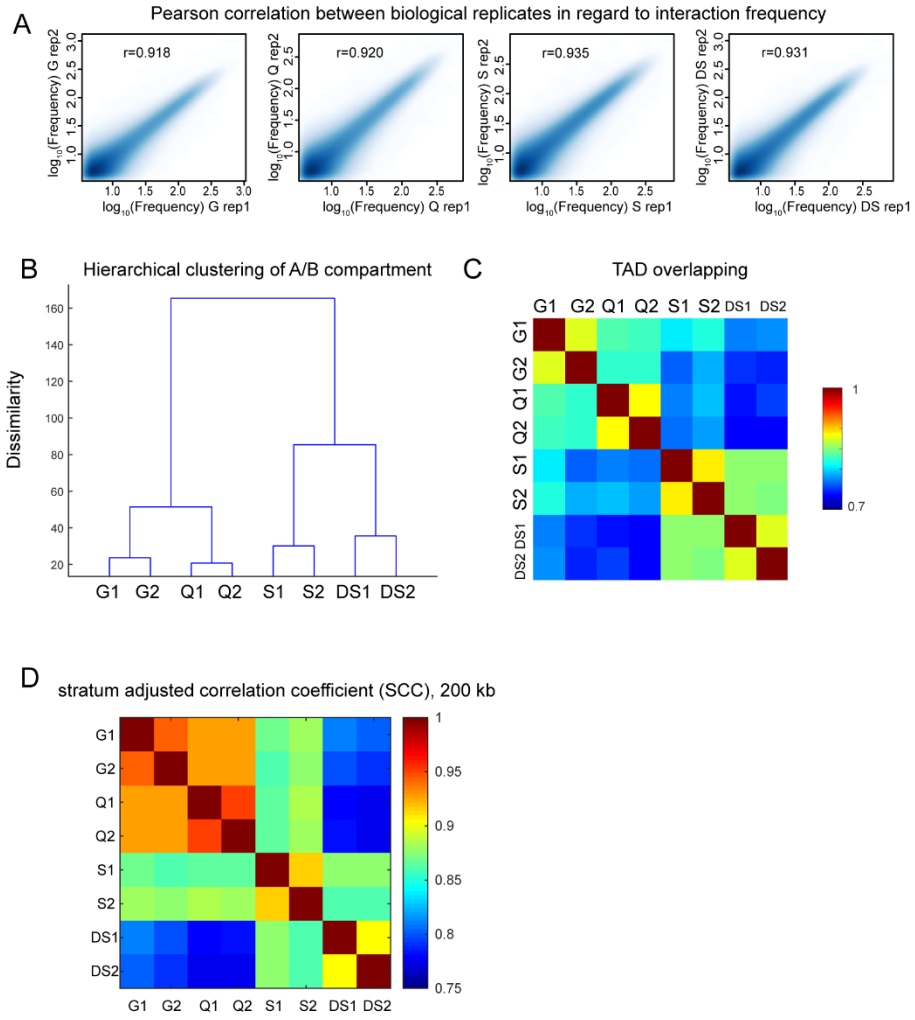

Figure S2. Reproducibility of Hi-C

(A) Density scatter plots for interactions of biological replicates in 100kb resolution. Pearson correlations were given.

(B) Hierarchical clustering of compartment scores at 40kb resolution.

(C) Proportions of overlapped TAD boundaries across biological replicates.

(D) Mean stratum adjusted correlation coefficient across all chromosomes calculated by HiCRep software with intra-chromosome contact at 200 kbp resolution.

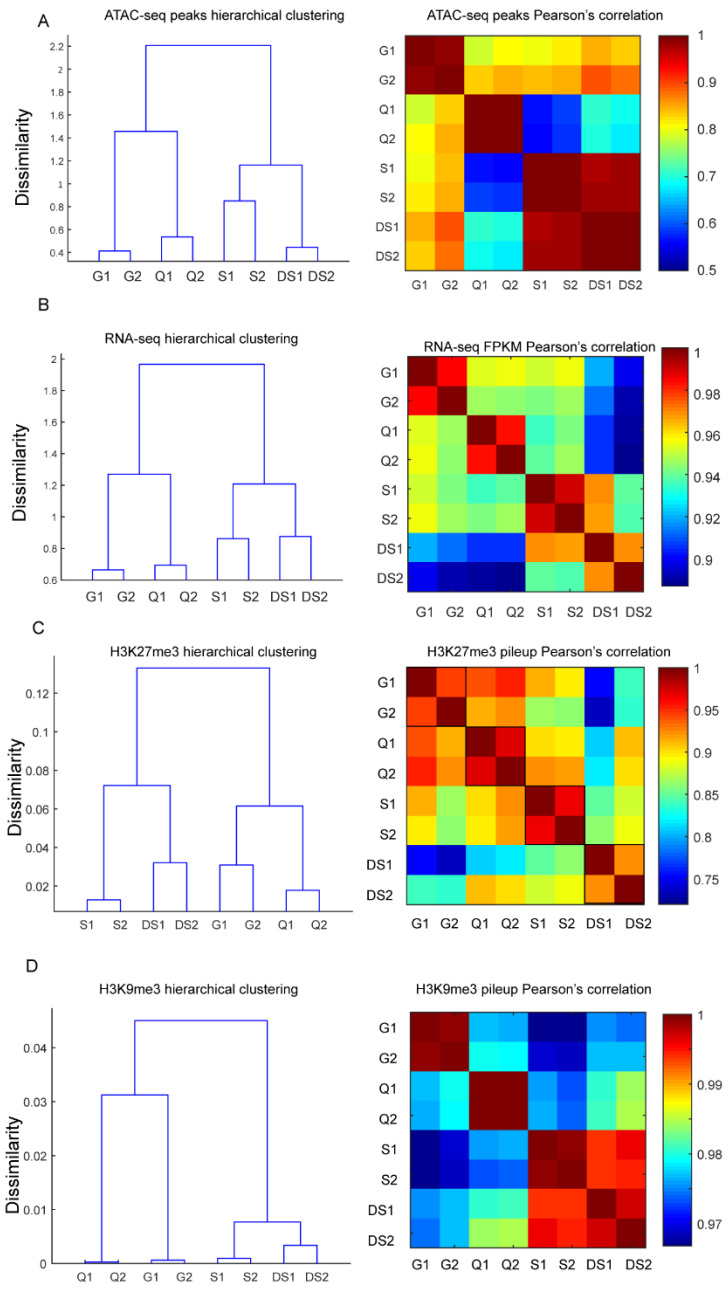

Figure S3. Reproducibility of ATAC-seq, RNA-seq and ChIP-seq

From A to D, Hierarchical clustering and Pearson correlation of biological replicates for ATAC-seq, RNA-seq, H3K27me3 ChIP-seq and H3K9me3 ChIP-seq. All biological replicates showed highly reproducible within each cell states.

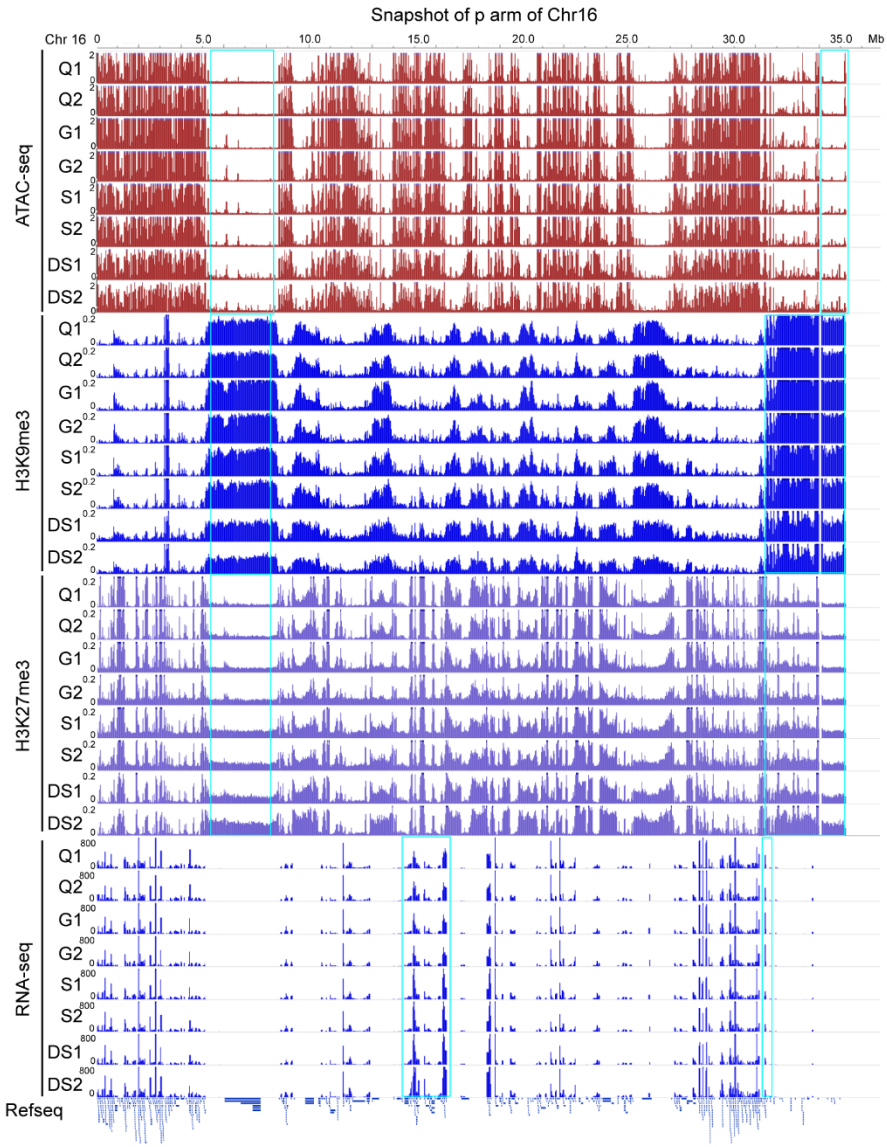

Figure S4. A snapshot of ATAC-seq, ChIP-seq and RNA-seq across biological replicates

The p arm of Chr 16 were shown. Boxes indicated regions showing differences across cell states. Biological replicates showed high reproducibility.

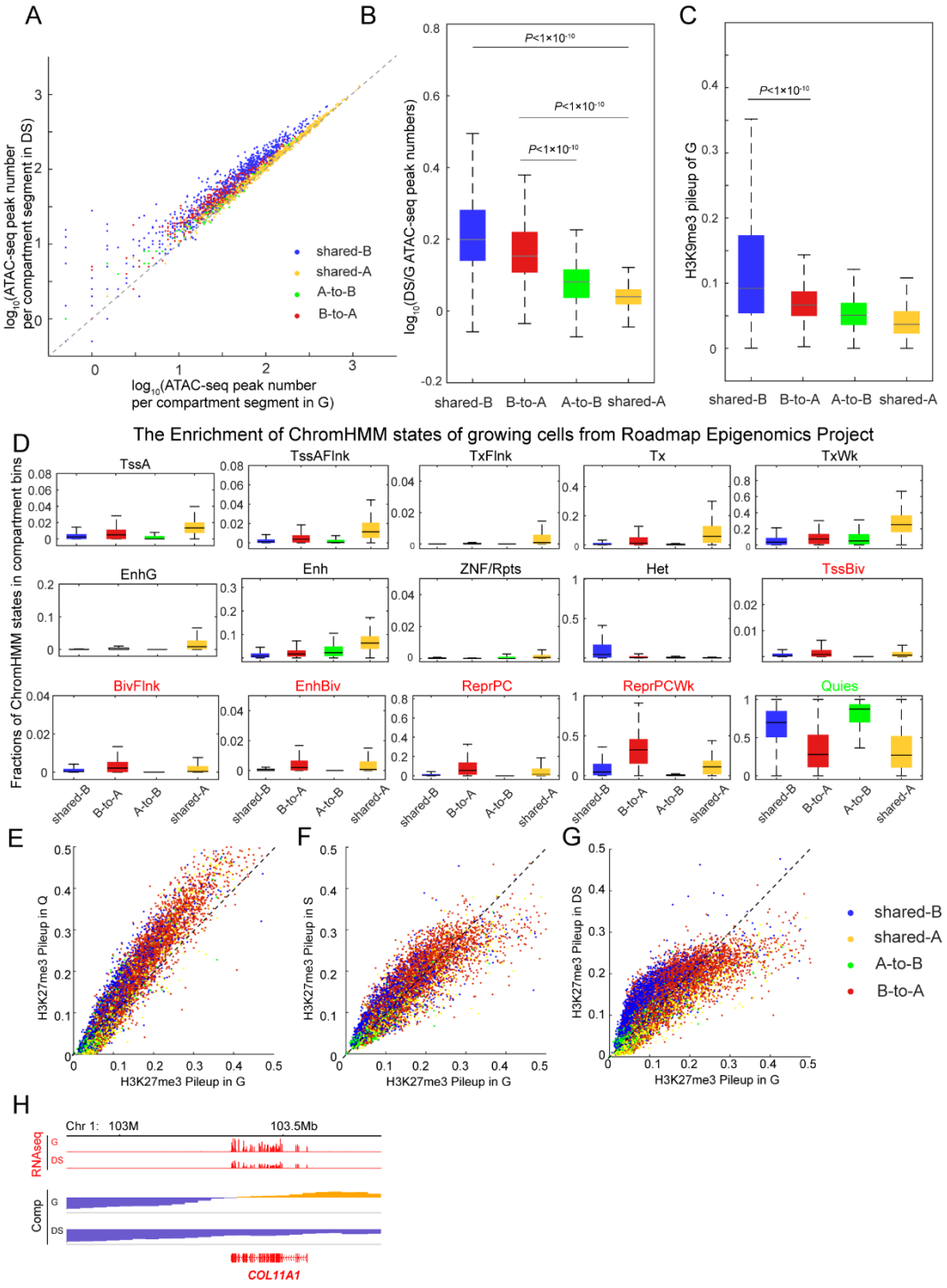

Figure S5. The relationship between compartment switching and chromatin accessibility, chromatin states and H3K27me, H3K9me3 profiles

(A) Scatter plot of ATAC-seq peak numbers per compartment segment in G and DS. Four categories are shared-B, A-to-B (de-active), B-to-A (de-repressed) and shared-A. In order to associate compartment switching with chromatin accessibility, we count the number of ATAC-seq peaks in each compartment segment. Compartment segment is defined as continuous bins with same A/B compartment sign. Segments whose size <= 200 kb (4 bins), which might be due to noises in calculation, were removed.

(B) Boxplots of log10 fold change of ATAC-seq peak numbers for four categories of compartment categories. Both shared-B and B-to-A regions showed increased accessibility.
(C) Boxplots of H3K9me3 enrichment in G for four compartment categories—Shared-B, B-to-A, A-to-B and shared-A. Shared-B and share-A were used as control group. Shared-B regions show significant higher enrichment of H3K9me3. Wilcoxon test was used to identify the statistical significance.
(D) Boxplots of the fractions of 15 kinds of ChromHMM states of growing cells in four compartment categories. B-to-A category was enriched in TssBiv, BivFlnk, EnhBiv states, whereas A-to-B category was enriched in Quies state. The chromatin states of foreskin fibroblast were from Roadmap Epigenomics Project. The active states consist of active transcription start site proximal promoter states (TssA, TssAFlnk), a transcribed state at the 5′ and 3′ end of genes showing both promoter and enhancer signatures (TxFlnk), actively transcribed states (Tx, TxWk), enhancer states (Enh, EnhG), and a state associated with zinc finger protein genes (ZNF/Rpts). The inactive states consist of constitutive heterochromatin (Het), bivalent regulatory states (TssBiv, BivFlnk, EnhBiv), repressed Polycomb states (ReprPC, ReprPCWk), and a quiescent state (Quies).
(E-G) Scatter plots of H3K27me3 pileups for G vs. Q, G vs. S and G vs. DS. Colors represented the types of bins. B-to-A regions maintained the relative high levels of H3K27me3 after senescence. While shared-B regions gained relatively high levels of H3K27me3 in S and DS.
(H) An example of deactivated genes. *COL11A1*, one of collagen genes, showed decreased gene expression and B-to-A compartment switching.

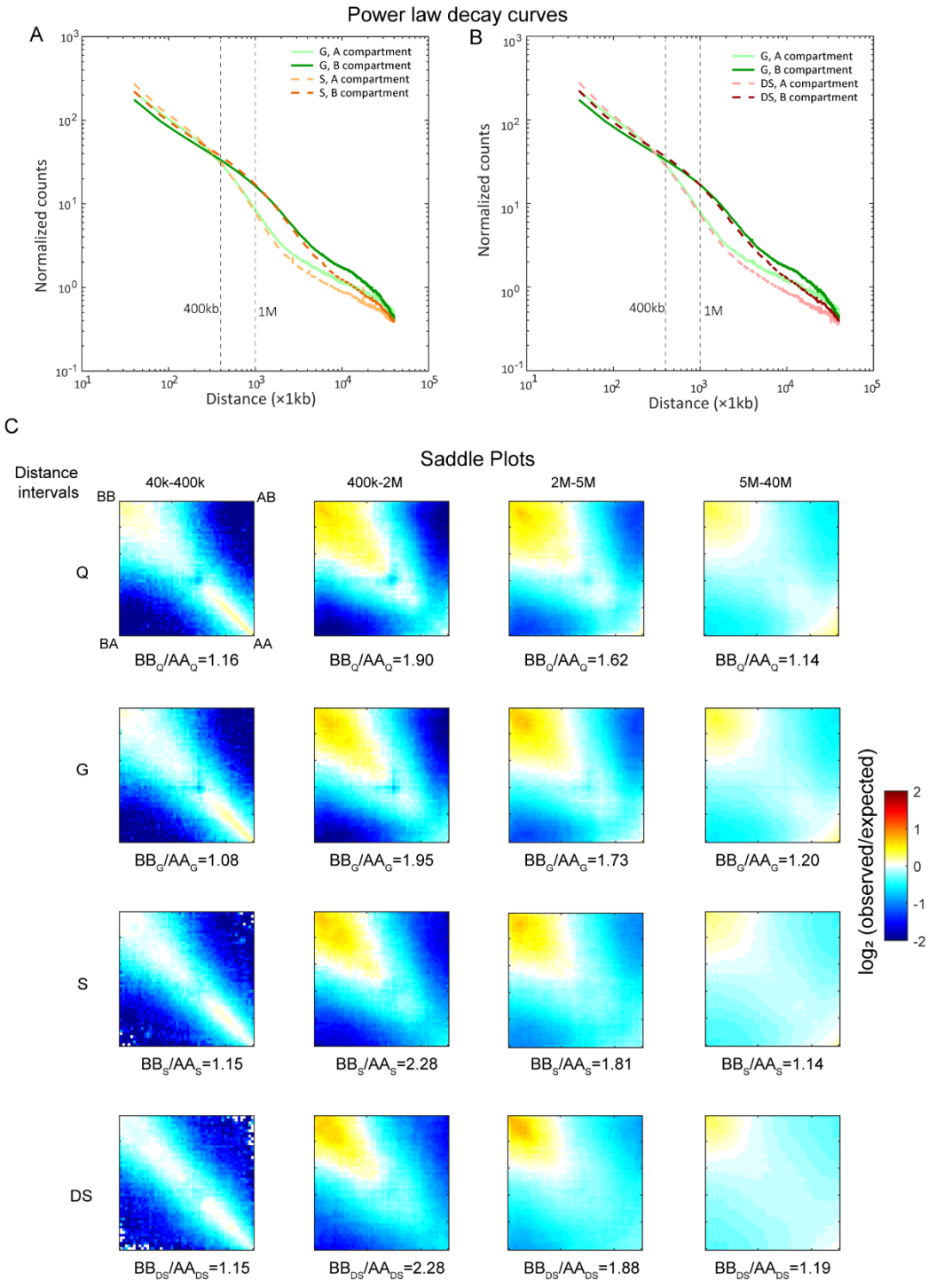

Figure S6. Comparisons of power-law decay curves and Saddle plots of A/B compartment

(A) The comparison of G and S. Interactions were divided into two types, A-A interaction and B-B interaction. Globally, S showed increased local interactions and decreased distal interactions for both of A-A and B-B.

(B) The comparison of G and DS. Interaction changes were similar to G versus S.

(C) Aggregated fold enrichment of interactions between A/B compartment. Compared with A-A interactions, B-B interactions gained relatively more interactions (400kbp-5Mbp).

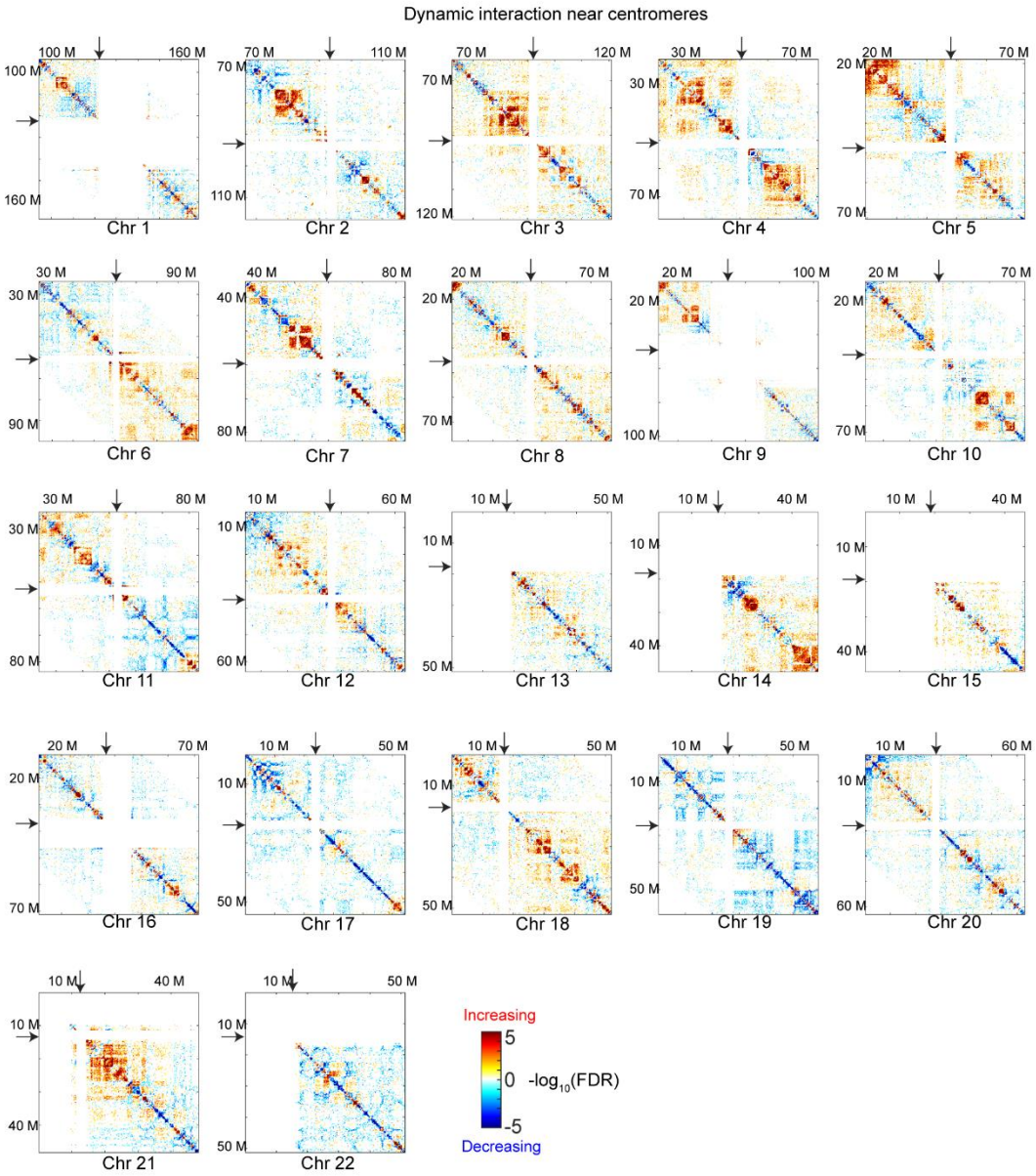

Figure S7. Differential interaction maps near pericentromeric regions for all autosomal chromosomes

The positions of centromeres have been labeled with black horizontal and vertical arrows. The increased interactions within ‘repressed’ regions were not dominated by the pericentromeric regions in most chromosomes.

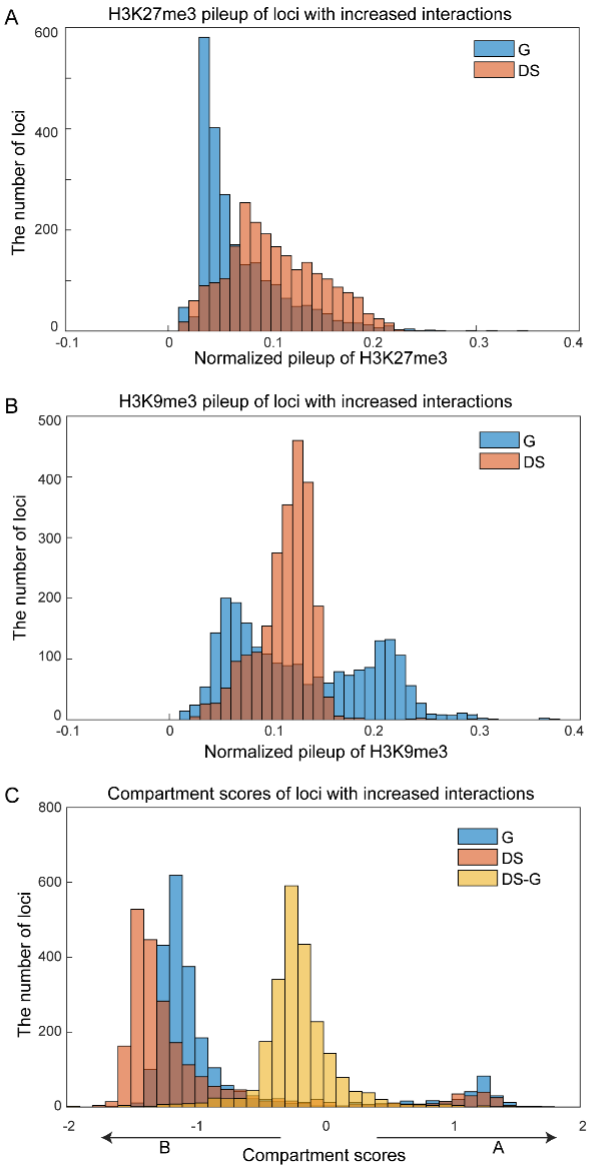

Figure S8. The distribution of histone modifications and compartment scores for loci with increased long-range interactions

(A) Histogram of normalized H3K27me3 pileup in G and DS for loci with increased long-range interactions. We calculated the numbers of significantly increased and decreased interactions for 200kb bins (FDR<0.01, distance > 1Mb). Bins showing higher numbers of increased interactions than that of decreased interactions ($N_{increased}/N_{decreased} > 2$), are then identified as loci with increased interactions. In DS, these loci showed increased H3K27me3 signal. (B) Histogram of normalized H3K9me3 pileup in G and DS for loci with increased long-range interactions. Many of these loci showed decreased H3K9me3 in DS. (C) Histogram of compartment scores in G and DS for loci with increased long-range interactions. Most of these loci showed stable B compartment in DS.

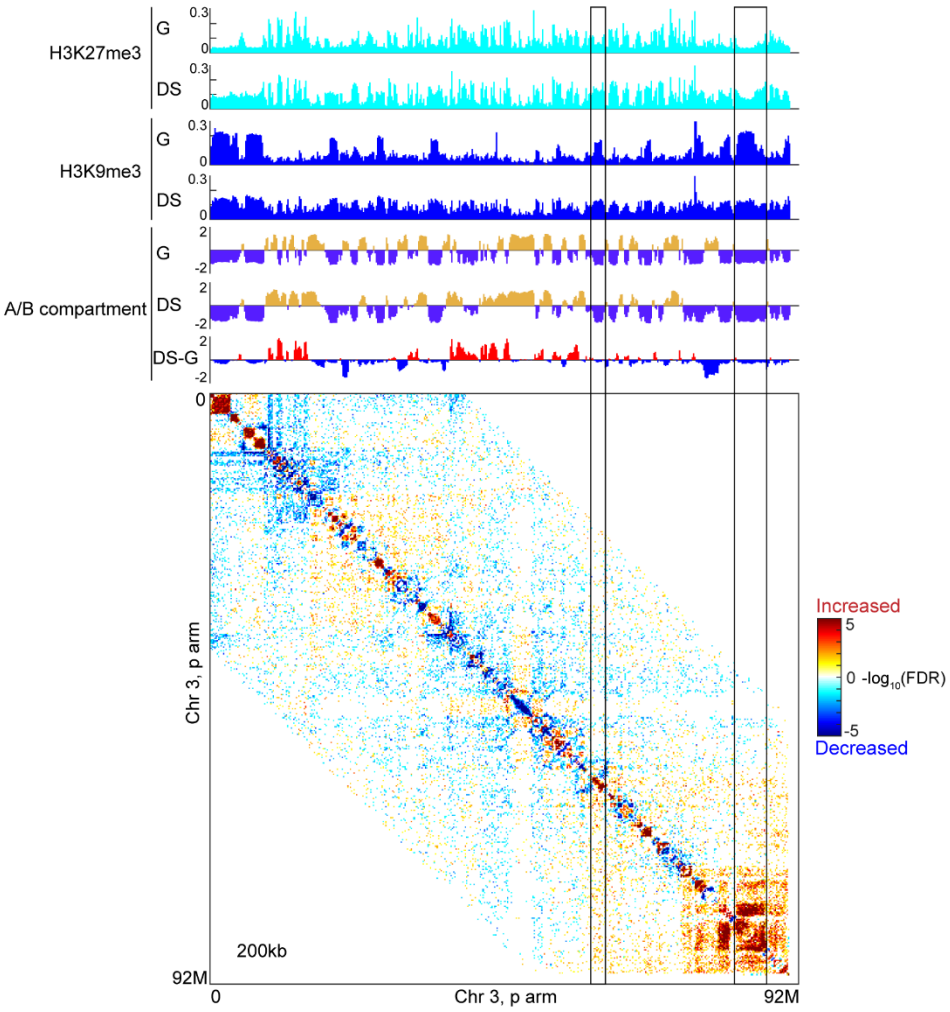

Figure S9. The example of p arm of Chr 3

Loci showing increased H3K27me3 and decreased H3K9me3 did not alter A/B compartment. The genomic region was same to Fig. 2E in the manuscript. The heatmap showed the differential interactions between DS and G.

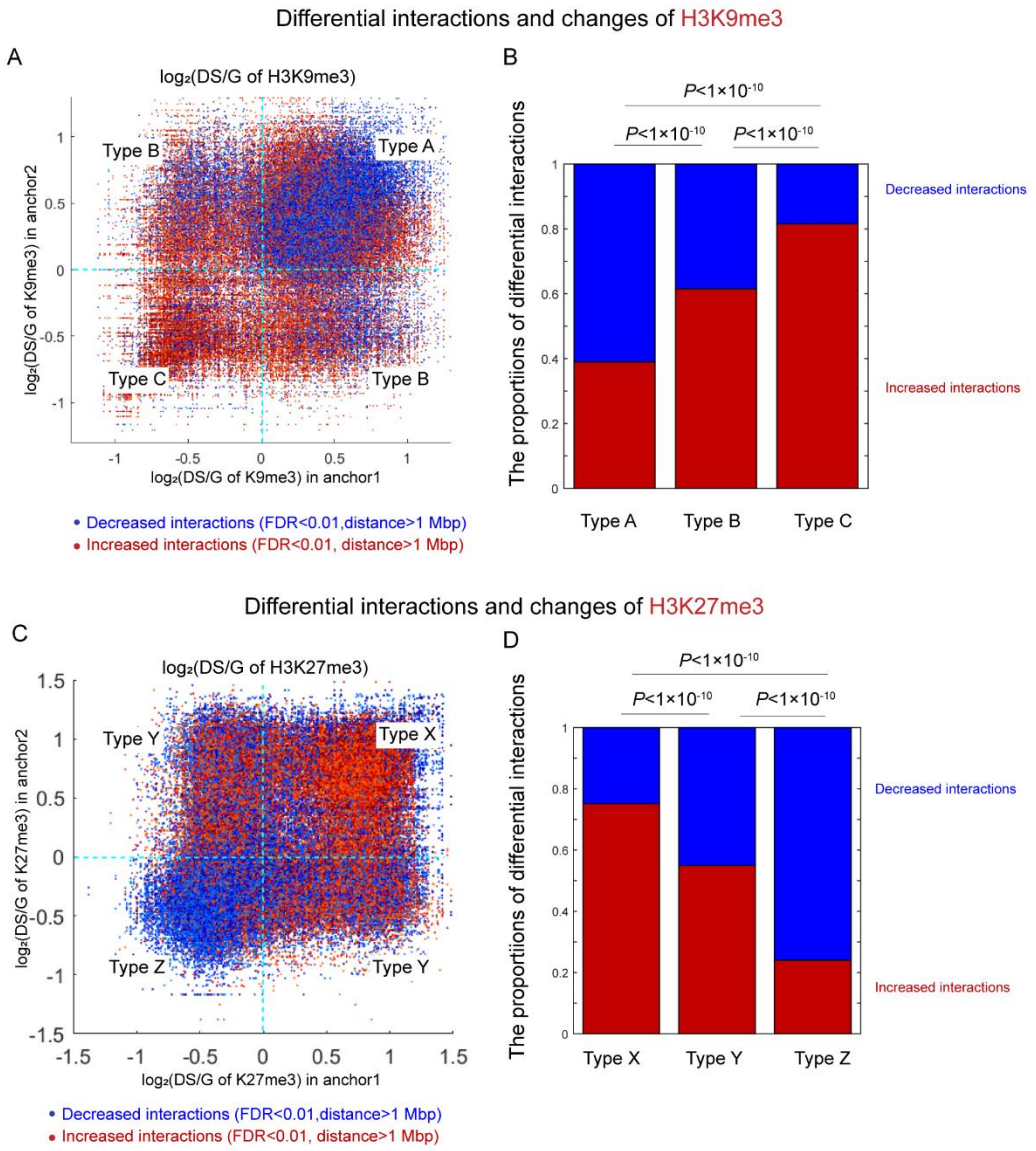

Figure S10. Anchors of increased long-range interactions enriched for relative decreased H3K9me3 and increased H3K27me3

(A) Scatter plots of fold changes of H3K9me3 between DS and G for two genomic anchors of differential interactions. Each point represents a significantly differential interaction (FDR < 0.01, Distance > 1 Mbp). Red represents increased interactions in DS, and blue denotes decreased interactions. Each interaction has two genomic anchors, whose fold changes of histone modification were shown as x and y coordinates, respectively. These plots could inform the relationship between the fold changes of histone modifications in two genomic anchors and the directions of differential interactions. Interactions are classified into three types (Type A, Type B and Type C). Type A represents interactions of H3K9me3 increased regions; Type B represents interactions between H3K9me3 decreased regions and H3K9me3 increased regions; Type C represents interactions of two H3K9me3 decreased regions.

(B) The composition of significantly increased and decreased interactions for three interaction types of panel A. *P* values were calculated by $\chi 2$ test.

(C) Scatter plots of fold changes of H3K27me3 between DS and G for two genomic anchors of differential interactions. Each point represents a significantly differential interaction (FDR < 0.01, Distance > 1 Mbp). Red represents increased interactions in DS, and blue denotes decreased interactions. Each interaction has two genomic anchors, whose fold changes of histone modification were shown as x and y coordinates, respectively. These plots could inform the relationship between the fold changes of histone modifications in two genomic anchors and the directions of differential interactions. Interactions are classified into three types (Type X, Type Y and Type Z). Type X represents interactions of H3K27me3 increased regions; Type Y represents interactions between H3K27me3 decreased regions and H3K9me3 increased regions; Type Z represents interactions of two H3K27me3 decreased regions.
(D) The composition of significantly increased and decreased interactions for three interaction types of panel C. *P* values were calculated by $\chi 2$ test.

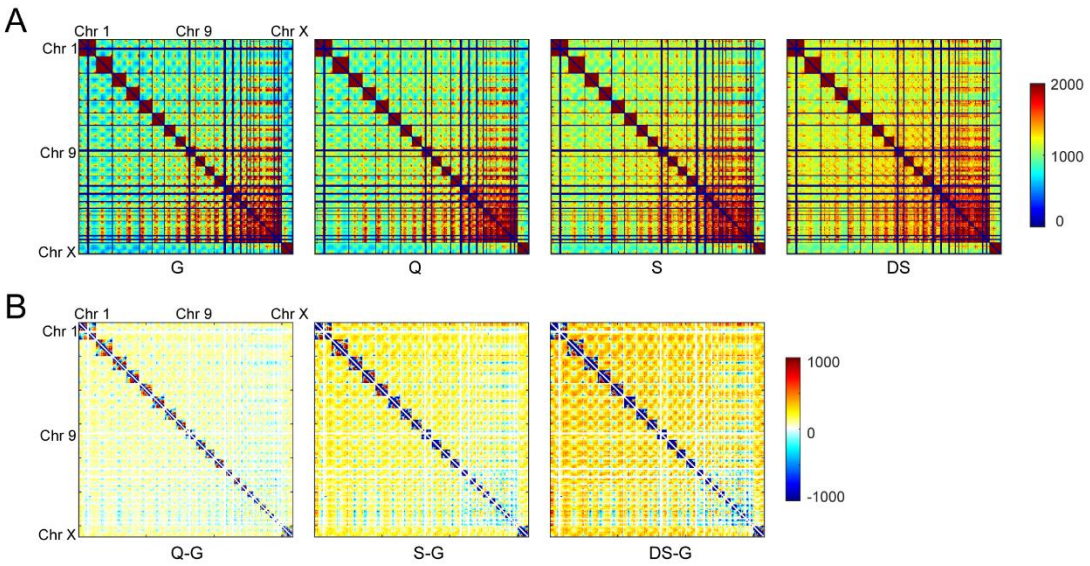

Figure S11. Whole genome contact maps and differential interactions

(A) The raw contact maps for G, Q, S and DS. Small chromosomes interact more frequently than other chromosomes in G.

(B) Differential contact maps by direct subtraction. Interactions between small chromosomes decreased during senescence.

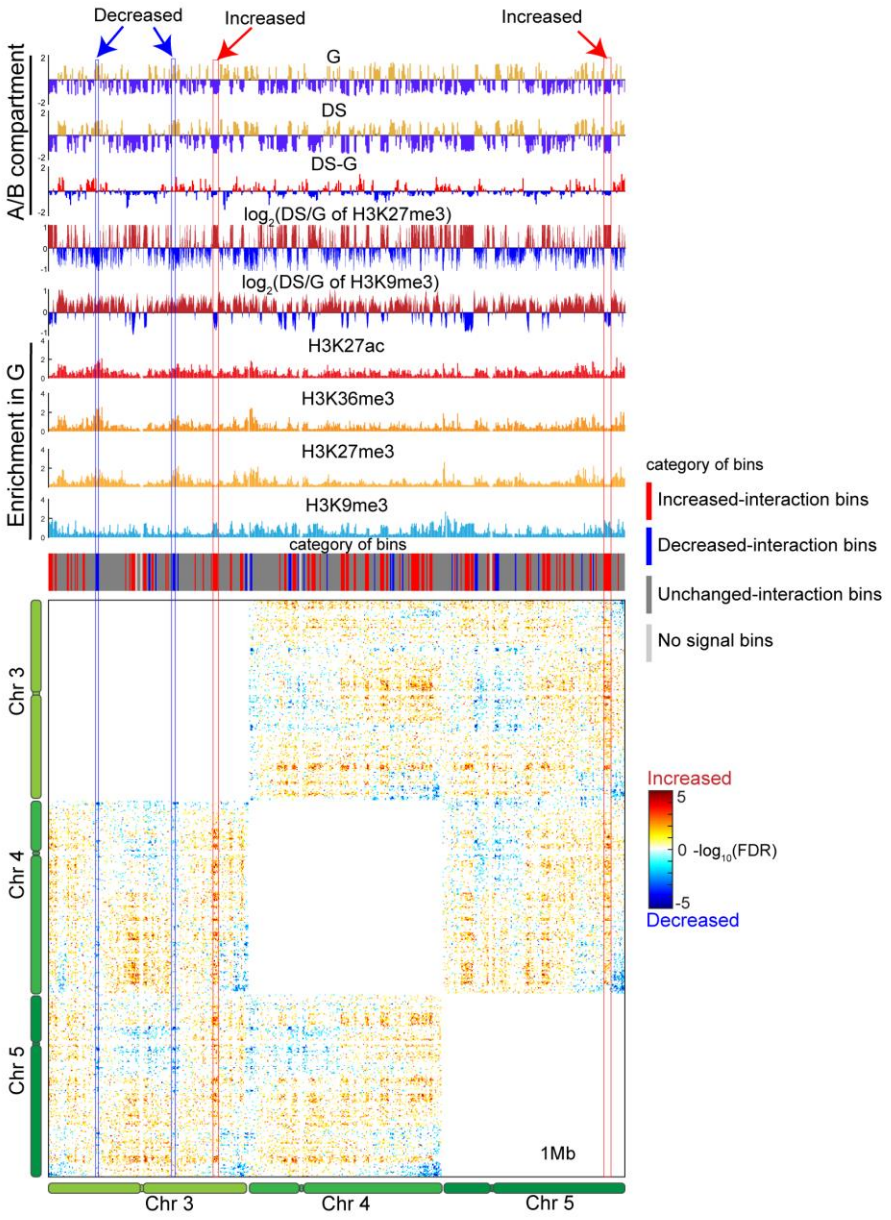

Figure S12. The example of interchromosomal interaction from Chr3 to Chr5

Loci showing interchromosomal interaction changes kept unchanged A/B compartment. The genomic region was same to Fig. 3B in the manuscript. Blue boxes indicated decreased-interaction bins, while red boxes indicated increased-interaction bins. They showed small changes of compartment scores.

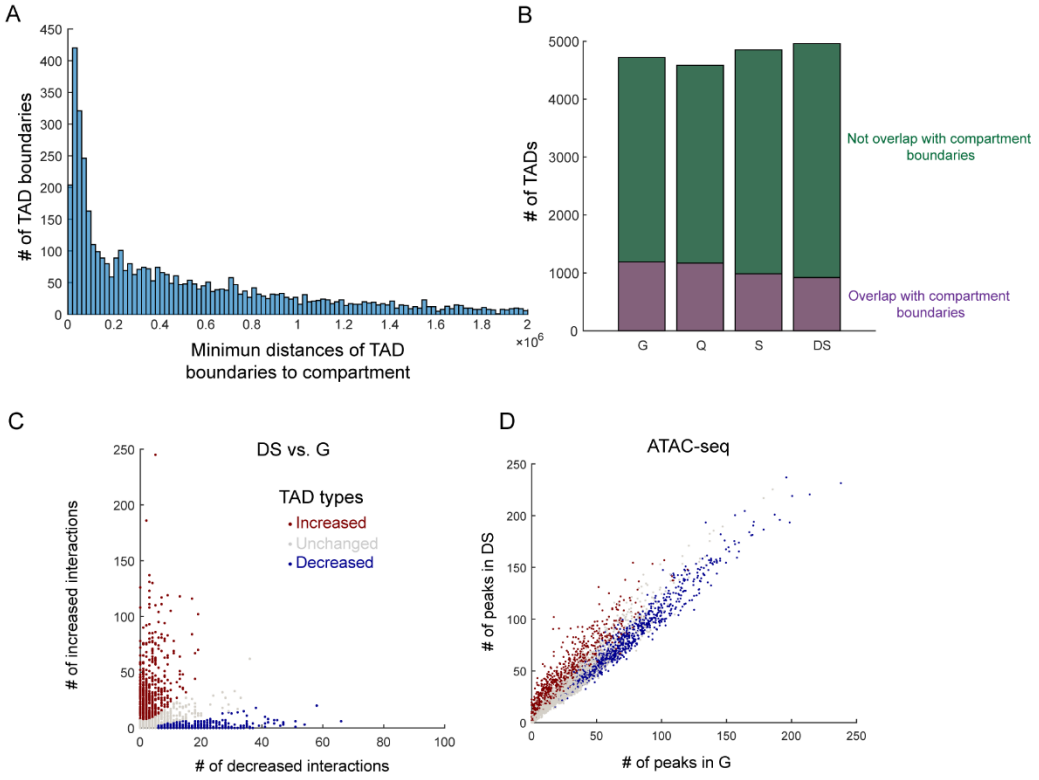

Figure S13. Re-analysis of TADs by ruling out compartment domains

(A) The distributions of minimum distances of TAD boundaries to compartment boundaries. There are a certain proportion of overlapping between two boundaries (distance < 60 kbp).

(B) The composition of TAD called by insulation scores according to whether TAD boundaries overlap with compartment boundaries. The majority of TAD boundaries are not overlapped with compartment boundaries.

(C) Scatter plot of the numbers of increased interactions and decreased interactions for TADs without the contamination of compartment domains.

(D) Scatter plot of the numbers of ATAC-seq peaks in G and DS for TADs without the contamination of compartment domains. TADs with increased intra-TAD interactions gained more peaks than decreased or unchanged TADs in DS (the mean ratios of DS to G for peak numbers are 1.08, 1.16, 1.87, corresponding to decreased-, unchanged- and increased-interaction TADs, respectively; Wilcoxon test, $P = 5.60 \times 10^{-231}$ for increased vs. decreased; $P = 7.51 \times 10^{-207}$ for increased vs. unchanged; $P = 3.10 \times 10^{-39}$ for unchanged vs. decreased).With filtered TADs, we performed the same analysis as before and found that the result was similar.

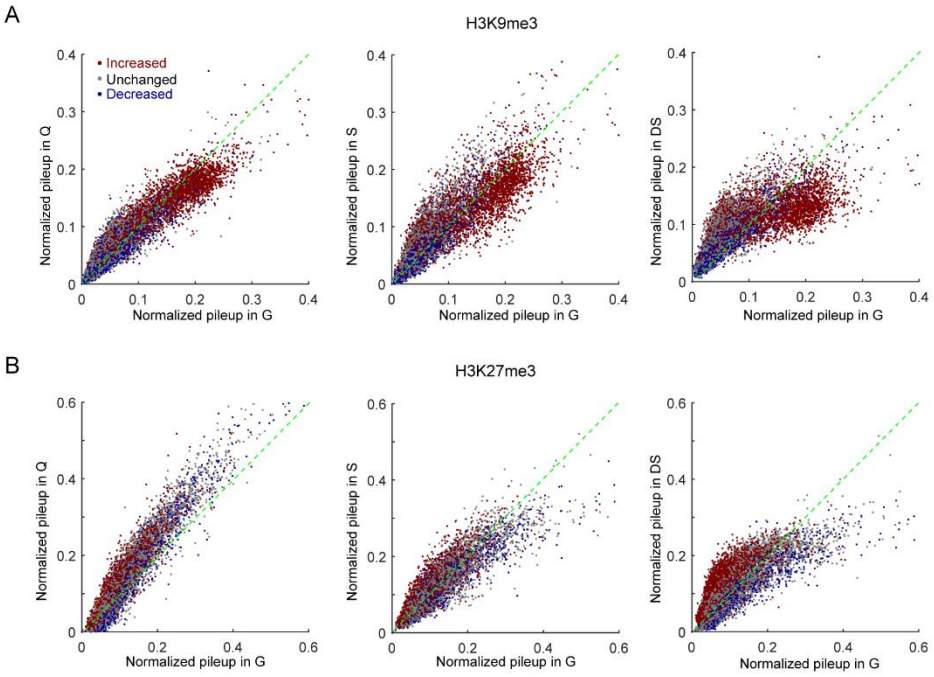

Figure S14. Changes of H3K9me3 and H3K27me3 associated with TAD interactions

(A) The comparison of H3K9me3 profiles between G and Q, G and S, G and DS. Each point represented a 10 kb bins belonging to different types of TADs, Increased-interaction TADs, Unchanged-interaction TADs and Decreased-interaction TADs. Compared with unchanged TAD bins, bins belonging to increased-interaction TADs showed much more clearly decreased H3K9me3 level in S and DS than Q.

(B) The comparison of H3K27me3 profiles between G and Q, G and S, G and DS. S and DS showed much more clearly increased H3K27me3 level for bins belonging to increased-interaction TADs than Q compared with bins of unchanged TADs.

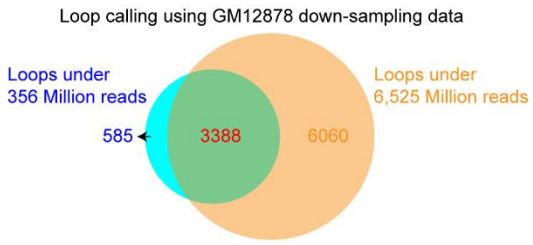

Figure S15. The Venn diagram for overlapped loops between extremely high sequencing dataset and down-sampling dataset

To examine the reliability of loops called under our sequencing depths, we down-sampled sequencing reads from published highest resolution data of GM12878 (Rao et al. Cell, 2014) to the similar depth (356M), and called loops on 20-kbp resolution contact maps. We obtained 3973 loops, out of which 3388 loops (85.3%) are overlapped with the loops called under extremely high sequencing depth. It was possible to miss some loops which could only be detected under extremely deep sequencing depths. However, comparing loops under the similar sequencing depths across four cell states was fair.

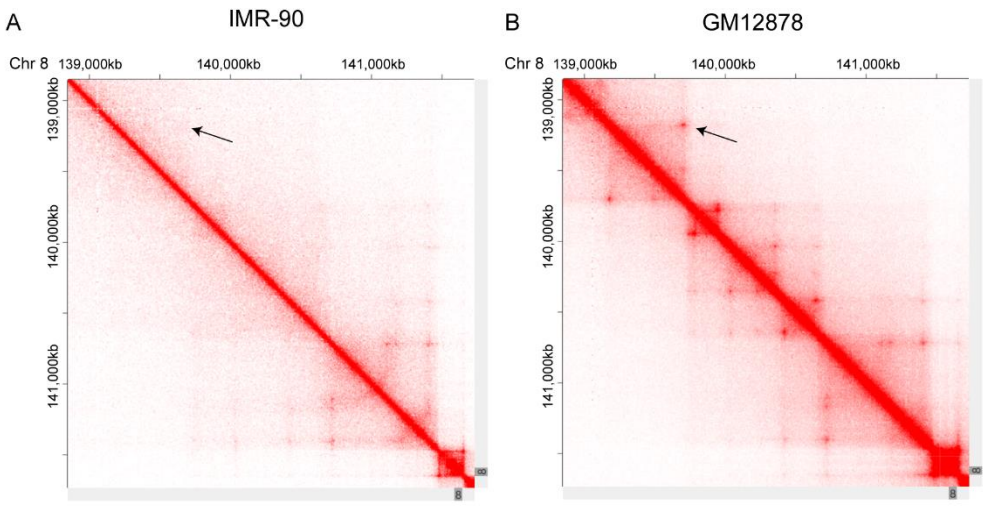

Figure S16. The interaction maps of IMR-90 (Panel A) and GM12878 (Panel B) cell lines from *Rao et al. 2014* around the loop of Fig. 5D, E.

The arrow pointed to the loop position. IMR-90 showed no loop, while GM12878 showed clear looping. The heatmap was from https://www.aidenlab.org/juicebox/.

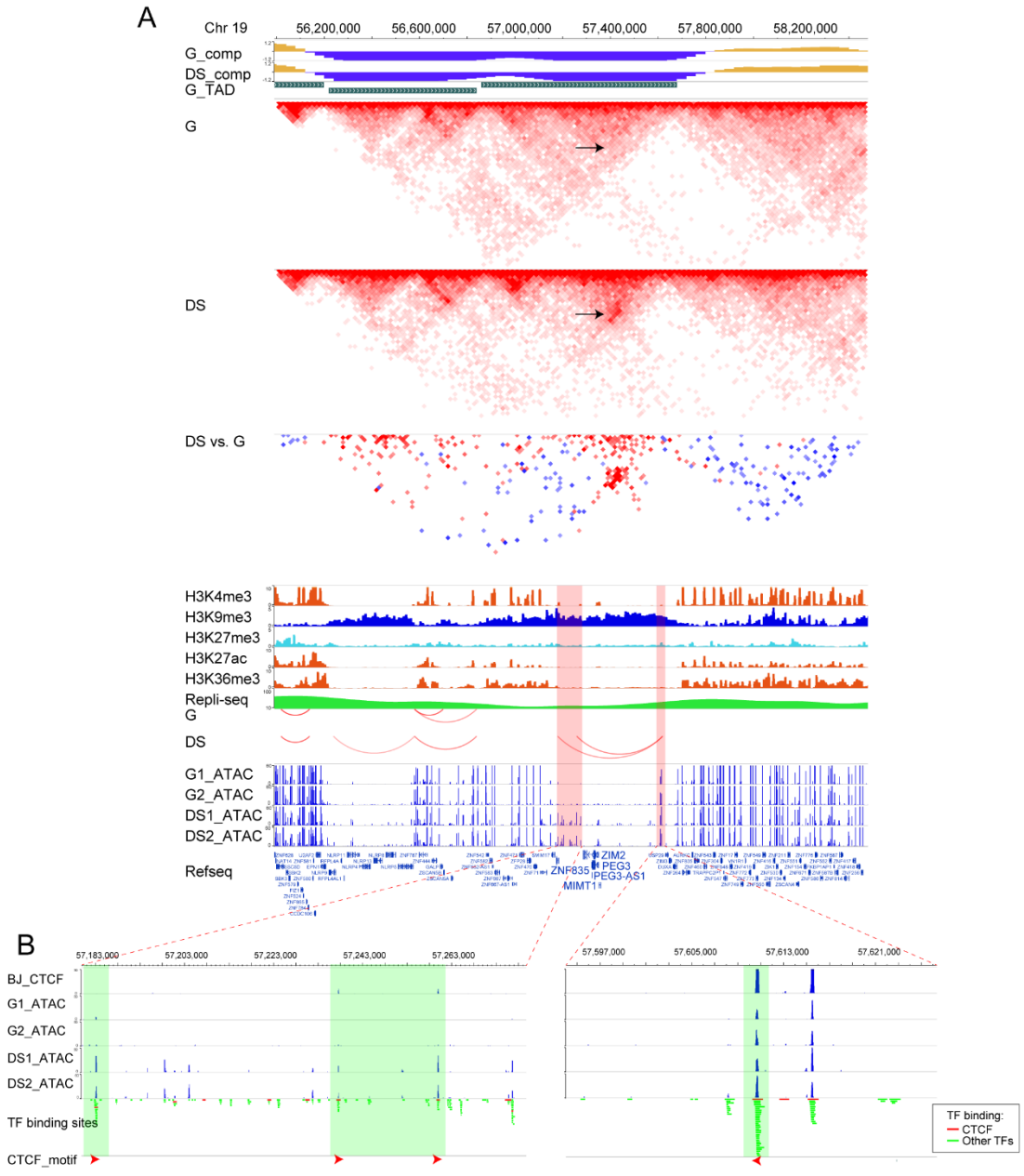

Figure S17. Browser view of an example of novel looping in heterochromatin of chr19

(A) Browser view of a genomic regions showing compartment scores, normalized contact map, dynamic interaction, histone modifications of G, loops and ATAC-seq signals.

(B) zoomed-in views of loop anchors. Tracks including BJ CTCF ChIP-seq, ATAC-seq, TF binding sites (red for CTCF, blue for other TFs) and CTCF motif orientations.

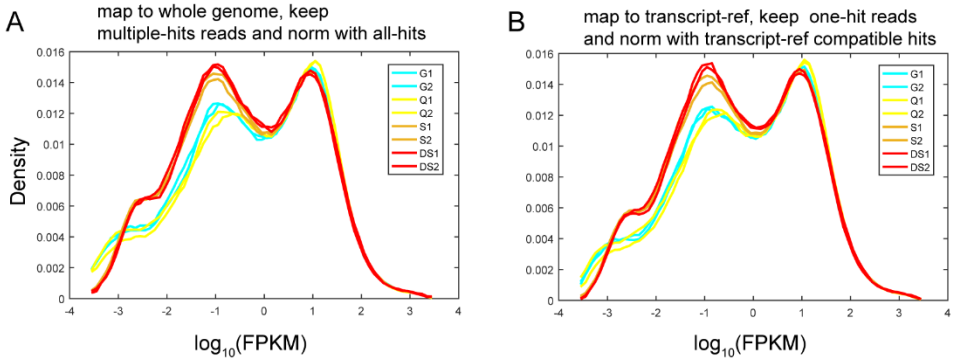

Figure S18. The distribution of gene expression by two different normalization methods

(A) The distribution of FPKM normalized by all mapped reads. (B) The distribution of FPKM normalized by one-hit and reference compatible reads. In the original pipeline (A), output of RNA-seq was mapped to whole genome allowing multiple-hits mapping, and was normalized by all hits reads when calculating FPKM. It is equivalent to taking the expression of repetitive elements into account. In order to evaluate the impact of normalization on gene expression leakage. We designed another pipeline to rule out repeat expression as much as possible. Output of RNA-seq was only allowed to map to transcription annotation reference with unique mapping parameter and was normalized by transcription-annotation-compatible hits when calculating FPKM. Two different normalization methods didn't affect the global distributions of gene expression, implying that gene expression leakage was not due to the bias of normalization

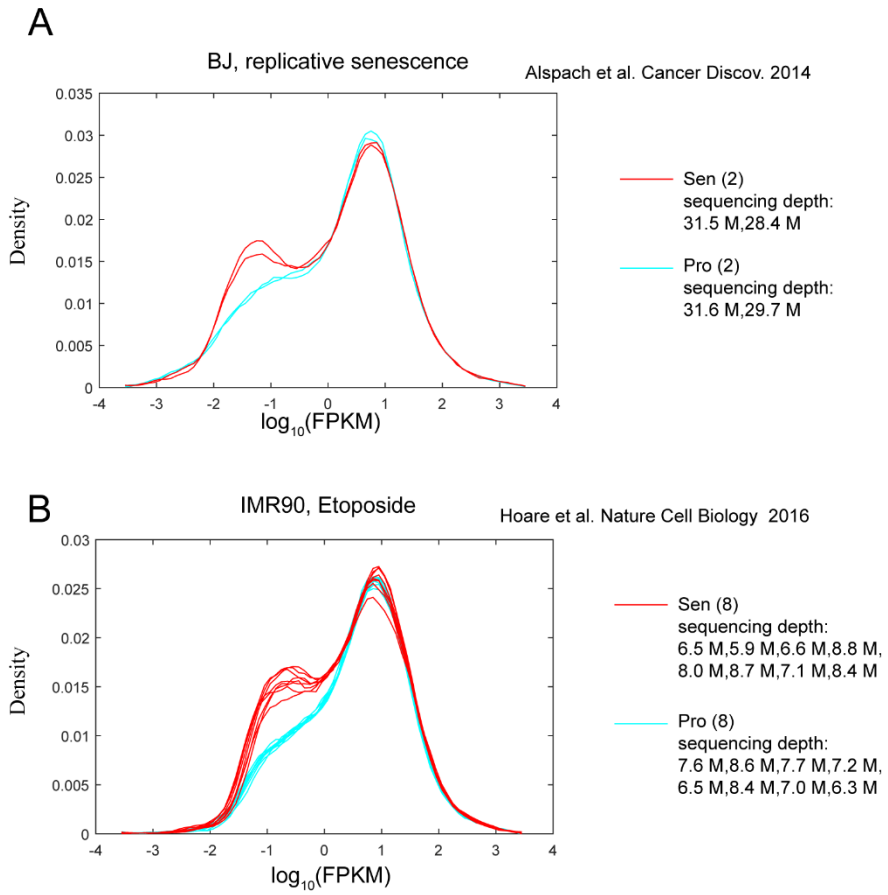

Figure S19. gene expression leakage observed in other cellular senescence datasets

(A-B) The distributions of gene expression in two published datasets. The sequencing depths were listed on the right. There were significantly higher fractions of low-expression genes in senescent cells, indicating there was gene expression leakage.

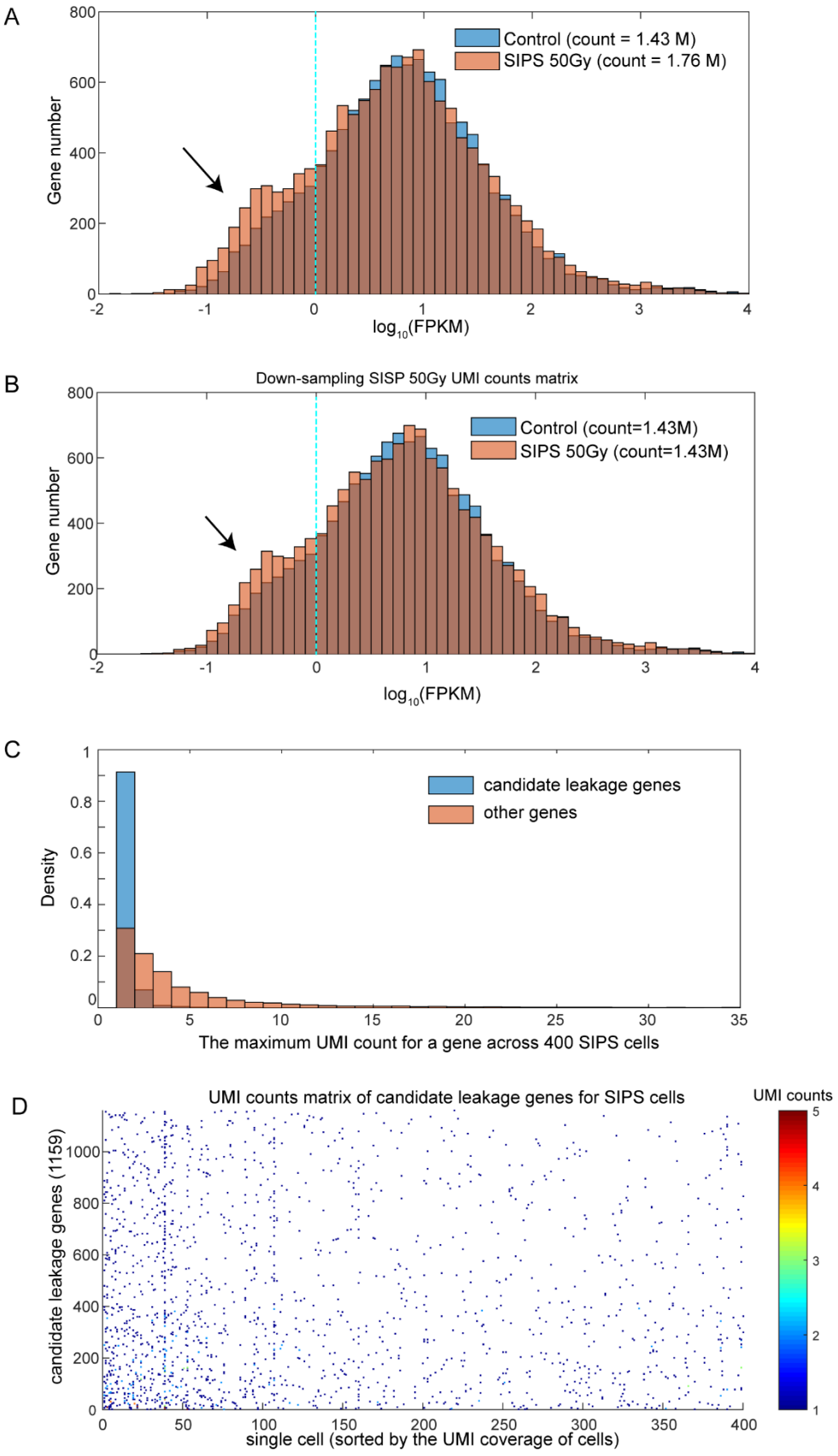

Figure S20. Gene expression leakage in single cells

(A) The distribution of $\log_{10}$(FPKM) for pooled single-cell RNA-seq. UMI coverages for control and SIPS were shown on the legend. There is significantly larger number of genes which showed low expression (0<FPKM<1) in SIPS. (B) Down-sampling SIPS count matrix to similar UMI coverage with control also showed expression leakage in SIPS. (C) The distribution of maximum UMI counts for each gene across 400 cells. Compared with other expressed genes, leakage genes showed lower maximum UMI counts. And most of leakage genes (99.8%) showed UMI counts < 5. This result suggested that most leakage genes was not likely to be a mix of highly expressed cells and no expressed cells. (D) The UMI counts matrix for candidate genes across 400 SIPS cells. The expression of leakage genes was low but widespread across SIPS single cells.

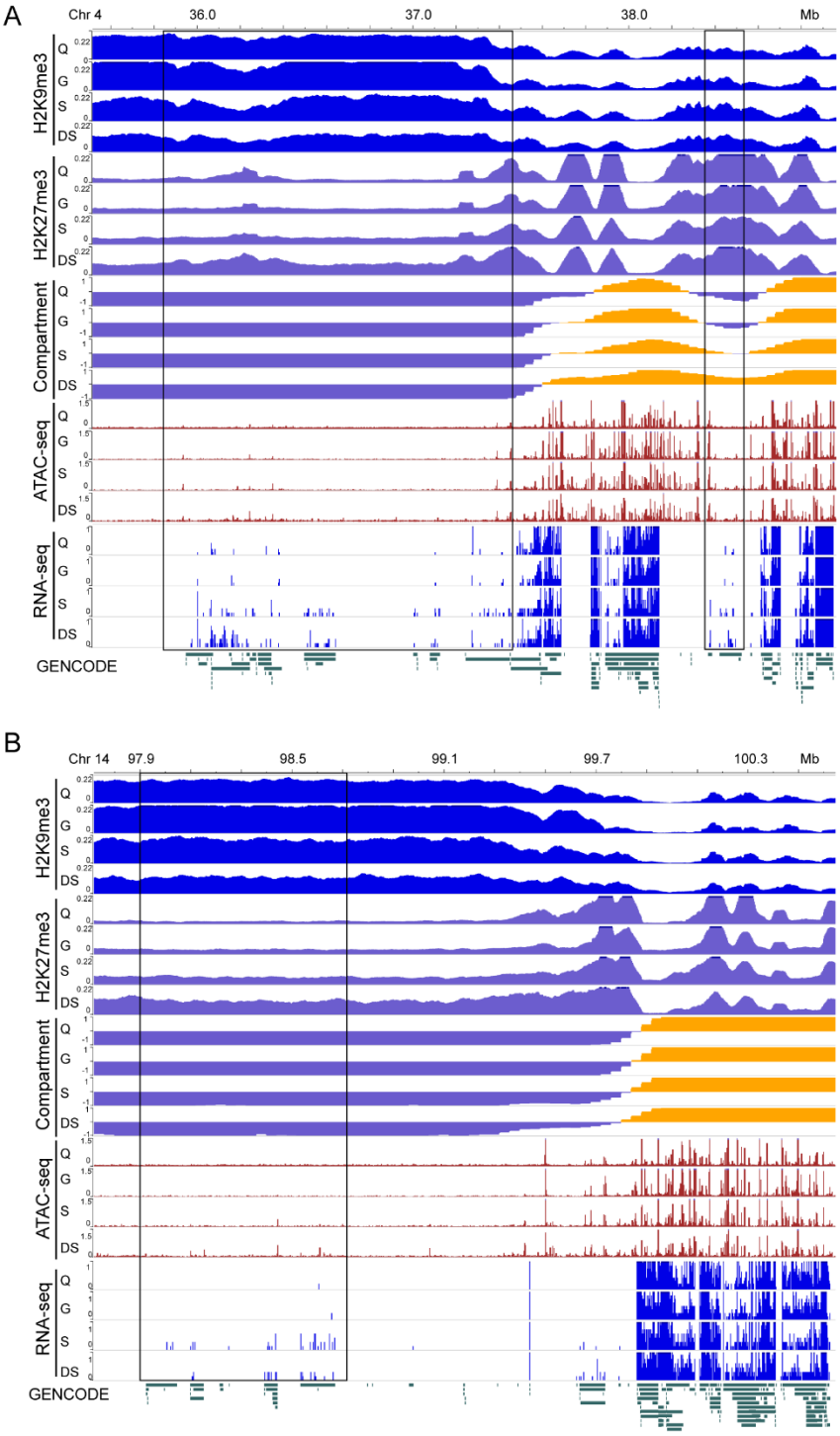

Figure S21. A snapshot of gene expression leakage

(A-B) Two examples of gene expression leakage. Black boxes showed gene expression leakage in H3K9me3 associated heterochromatin or B-to-A regions. The maximum of RNA-seq scale was very low in order to be suitable for showing the expression level of 'leakage' genes.

The crosstab between gene expression changes and local interaction changes with each TAD as a unit

TAD types	Down-exp TADs	Up-exp TADs
Decreased TADs	425	561
Unchanged TADs	755	1293
Increased TADs	118	570

Figure S22. The local interactions within TADs were related to gene expression changes

We defined up-expressed and down-expressed TADs by comparing the numbers of consistently up-regulated and down-regulated genes in each TAD (when $N_{up} > N_{down}$, the TAD is defined as up-expressed TAD; when $N_{up} < N_{down}$, TAD is defined as down-expressed TAD). When gene expression in two replicates of one cell state is consistently higher or lower than two replicates of another state, the gene is defined as consistently up-regulated or down-regulated genes. If there are no differences between three types of TAD, the ratios of up-regulated genes to down-regulated genes should be similar across TAD types. However, we found that three different TAD types show different ratios. Ratios of up-regulated TAD number to down-regulated TAD number are 1.32, 1.71 and 4.83 for decreased-, unchanged- and increased-interaction TADs ($\chi 2$ test, $P < 2.2 \times 10^{-16}$). Therefore, gene expression leakage is significantly different among the three types of TADs.

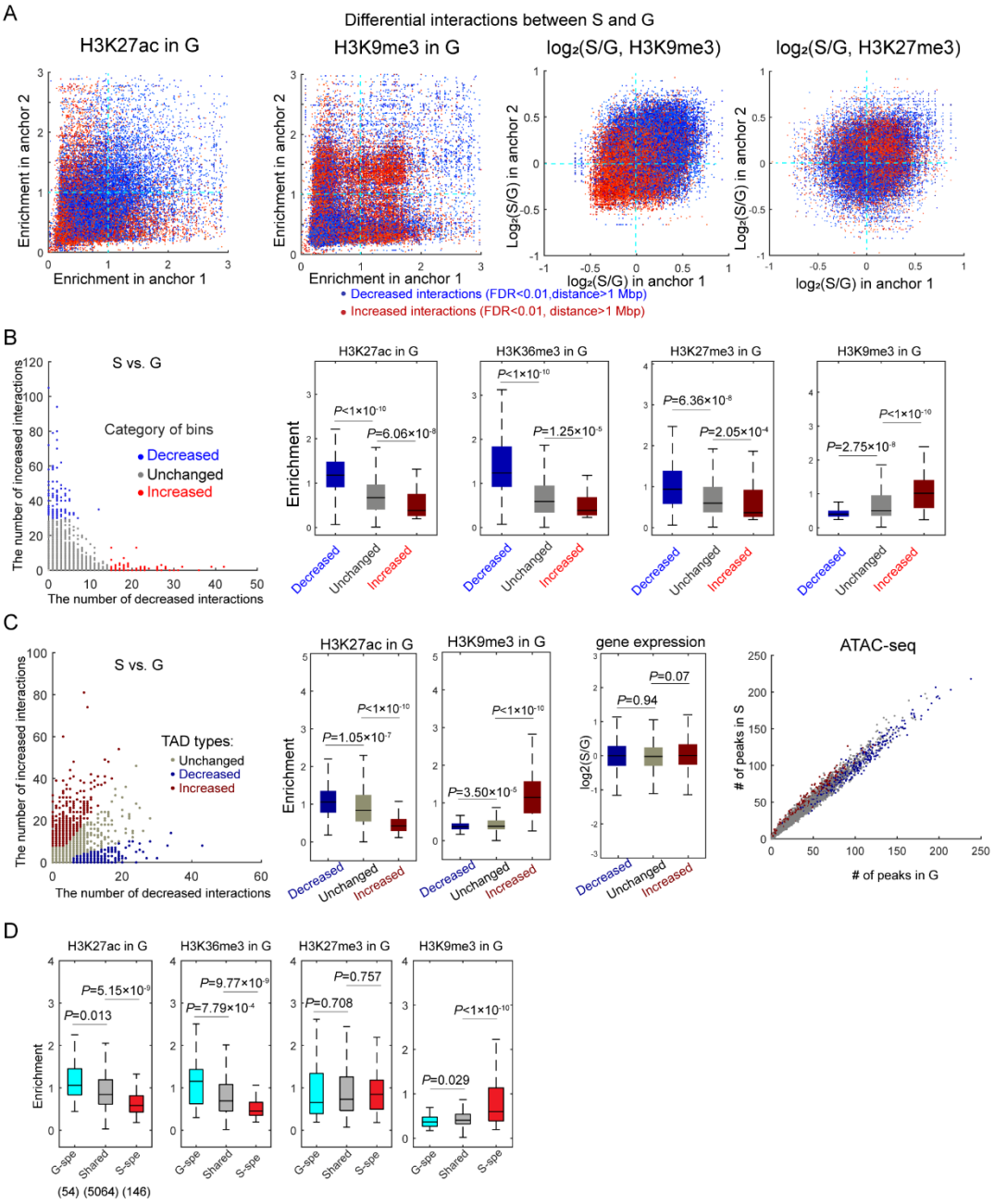

Figure S23. Senescent cells shared similar but relatively weak changes to deep senescent cells

(A) Analysis of differential interactions at 200 kb resolution for S versus G.

(B) Analysis of differential interchromosome interactions for S versus G.

(C) Analysis of differential intra-TAD interactions for S versus G.

(D) Enrichment of histone modifications for G and S specific loops.

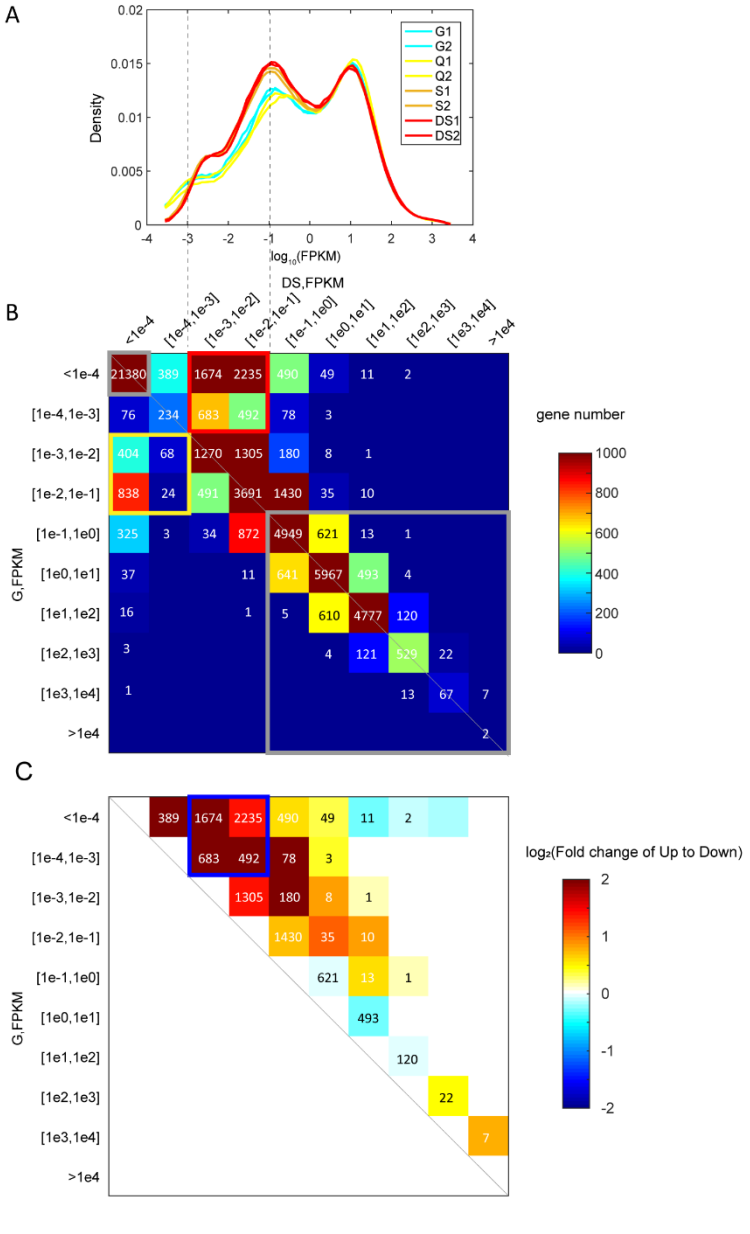

The proportion of genes whose promoters overlapped with ATAC-seq peaks

Genes type	Leakage (3160)	Silence (11990)	Expressed (4218)
Fractions of overlapping G1 peaks	0.1925	0.1140	0.7137
Fractions of overlapping G2 peaks	0.2246	0.1275	0.7259
Fractions of overlapping DS1 peaks	0.3093	0.1921	0.7414
Fractions of overlapping DS2 peaks	0.3113	0.1926	0.7366
Gained peaks percentage	10.2%	7.2%	1.9%

Figure S24. The source of leakage genes in deep senescent cells

(A) The distribution of gene expression.

(B) The matrix showing the distribution of gene expression across G and DS, where each element represents the number of genes (numbers and colors on the plot both represent gene numbers).

(C) $\log_2$(Fold change) for symmetric elements along diagonal of panel B. Color represents $\log_2$(fold change), while numbers on the plot are the gene numbers on the top of diagonal of panel B.
(D) The proportion of genes whose promoters gained accessibility.

First, we tried to identify leakage genes. Leakage genes occupy only a small fraction of genes whose FPKM is within 10^{-3} to 10^{-1} and including all genes within 10^{-3} to 10^{-1} will increase the false positive ratio. Thus, we try to identify the source of leakage genes during senescence. We draw a transformation matrix showing the numbers of genes satisfying different intervals of FPKM in G and DS. For panel B, each element shows the number of genes satisfying the FPKM intervals both in G and DS. Elements within the top of diagonal represent the numbers of up regulated genes, and elements within the bottom of diagonal represent down regulated genes. Genes whose FPKM are within 10^{-3} to 10^{-1} in DS have three sources: up regulated genes (red box in **B panel**), unchanged genes, down regulated genes (yellow box in **B panel**). Since unchanged genes won't change the proportion of leakage genes, we speculated that up regulated genes or down regulated genes will be the source of leakage genes. We calculated fold changes of symmetric elements along diagonal (**C panel**) and find there is 3.81-fold change for the number of up regulated genes to that of down regulated genes (blue box in **C panel**). So we regard genes whose FPKM in G are $< 10^{-3}$ and FPKM in DS are within $1e^{-3}$ to $1e^{-1}$ as leakage genes. Since we have shown that B compartments are enriched for leakage genes (Fig. 6B in the revised manuscript), thus we only used genes within B compartment for the following analysis. Even we included genes from A compartment, the result was similar.

Second, to assess the changes in chromatin accessibility of leakage gene promoters, we included two control gene sets: silence genes (FPKM $< 1 \times 10^{-4}$ for both G and DS, grey box on the top left of **B panel**), expressed genes (FPKM>0.1 for both G and DS, grey box on the bottom of **B panel**). Leakage genes and two control sets were used when their promoters were within B compartment. Then we calculated the factions of genes whose promoters are overlapped with ATAC-seq peaks (**D panel**). We found that, although leakage genes gained much higher percentage of peaks than expressed genes (10.2% vs. 1.9%), silence genes show similar percentage with leakage genes (7.2% vs. 10.2%). Furthermore, the proportion of leakage genes overlapping DS peaks was low (31%). It shows that increased accessibility within promoters of leakage genes cannot solely explain the emergence of gene expression leakage.

At last, 96.33% of gained peaks in DS were annotated as intergenic regions or intron. So increased accessibility in the promoters of leakage genes also cannot explain the gained peaks in the genome of DS.

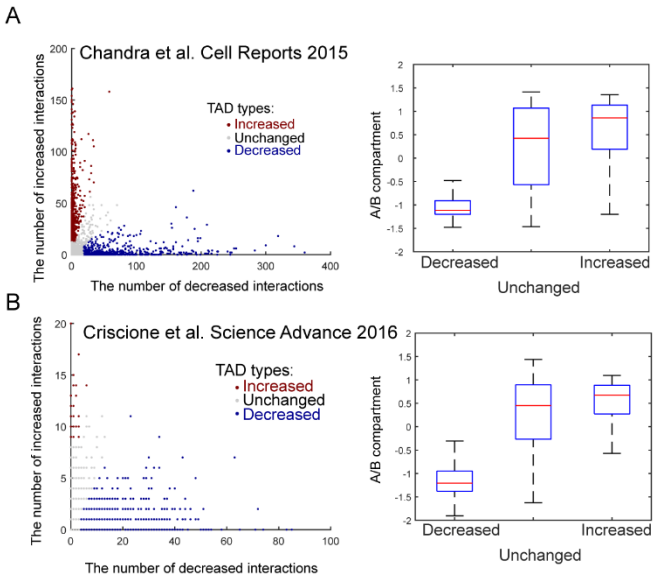

Figure S25. Re-analysis of two published Hi-C datasets.

(A-B) Left: The scatter plots of the numbers of increased interactions and decreased interactions within the same TADs. Right: boxplots of compartment scores for three different TAD types.

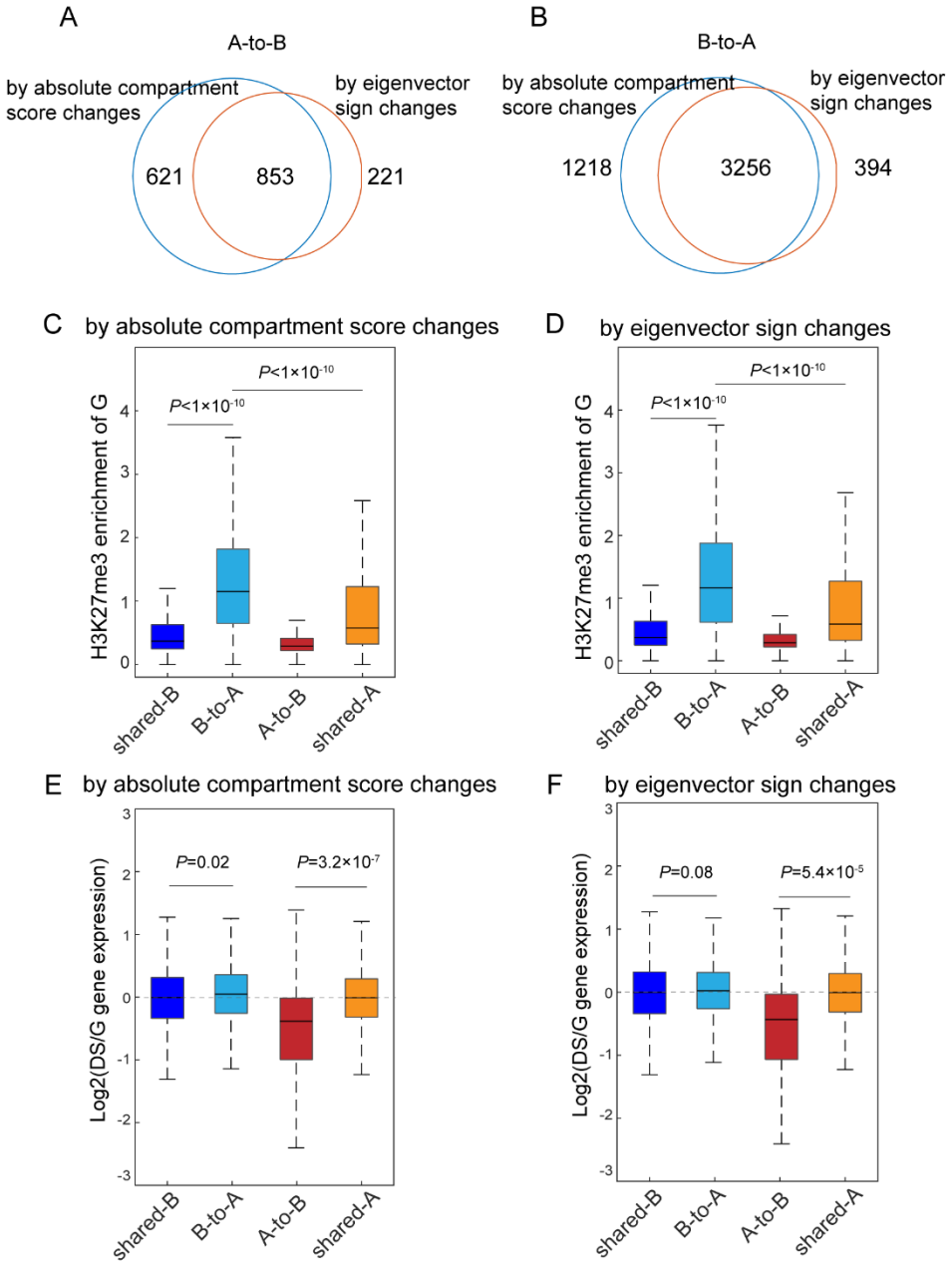

Figure S26. The comparison of two methods calling compartment switching

(A-B) We compared two methods (by eigenvector sign changes and absolute compartment score changes (absolute diff>0.75)) for calling compartment switching. Switching compartments identified by these two methods were largely consistent. The Venn diagram of A-to-B (A) and B-to-A (B) compartment for two methods. Each 40kb bins was considered as a unit. (C-D) The enrichment of H3K27me3 in G for different compartment categories. *P* values were calculated by Wilcoxon test. (E-F) The fold change of gene expression for different compartment categories. *P* values were calculated by Wilcoxon test.